Employing Boundary Element Approach With Genetic Algorithm to Increase Travel Range of Repulsive Actuators

Yu Tian, Ronald N Miles, Shahrzad Towfighian

Abstract—**The design of repulsive electrostatic actuators having enlarged travel range is achieved by combining the boundary element approach and a genetic algorithm. The boundary element method enables calculating the electrostatic forces without time consuming finite element simulations. Once a static equation that uses a model of effective lumped mass solves the travel ranges, the GA maximizes travel ranges by optimizing the dimensional parameters. The effectiveness of the scheme is demonstrated with extensive experimental results showing the travel ranges of a micro out-of-plane actuator are increased by up to 190%. The developed platform can improve the signal-to-noise ratios and the performance of general multi-electrode systems.**

Index Terms—**electrostatic MEMS, out-of-plane actuator, optimization, boundary element approach, genetic algorithm**

I. INTRODUCTION

THE employment of out-of-plane actuators in microelectromechanical systems (MEMS) is found in applications of switches and attenuators [1]–[5], high-resolution displays [6]–[8], and maskless lithography [9]–[11]. Micro-actuators can be driven by electrothermal, piezoelectric, electromagnetic, and electrostatic mechanisms. During the past few decades, electrostatic actuation has attracted broad attention because it has tremendous advantages over other mechanisms. The electrostatic actuators are compatible with IC processes because they use voltage sources in the electronic circuits to generate electric fields. Electrostatic actuators consume very low amounts of power ($<$1mW) and only when they are moving out-of-plane to connect circuits (e.g., switching to the ON state). The developed micro machining technologies make out-of-plane micro actuators easy to fabricate for diverse structures and meet various needs in different optical applications. In the scheme of electrostatic actuation, the out-of-plane movements are controlled by the electrostatic forces. If the out-of-plane movements are translational, the actuators can statically or dynamically make and break electric circuits and often work as switches. With rotational movements driven by electrostatic forces, the out-of-plane movements of actuators can accomplish many tasks; for example, in an array of micro mirrors they can adjust the reflection of incident lights precisely to target angles and steer the optical paths.

Because of the nature of electrostatic actuation, the travel ranges of out-of-plane actuators depend on the levels of applied voltages. The speed of travel is related to the rate of change of the voltages. Meanwhile, the travel range must be constrained to a range that does not allow unstable out-of-plane motions, which would lead to unpredictable, uneven, and unreliable actuation. Because a large travel range allows an out-of-plane electrostatic actuator to be used for more tasks, much effort has been put into expanding the range. For the out-of-plane actuators of classic parallel-plate designs, the primary limitation is that the two electrodes unavoidably collapse when the displacement is driven beyond 30% of the initial gap. Strategies to mitigate pull-in instability include devising deformable actuators [12] or applying flexible connecting structures such as levers [13], integrated torsional flexures [14], and rotation transformers [15]. They all exhibited efficiency but could not avoid the inevitable collapsing of the two electrodes. Control-based techniques [16]–[18] can adjust the parasite capacitance before the pull-in instability and slightly improve the travel range for electrostatic out-of-plane actuators. However, none of them eliminates the pull-in instability that fundamentally limits the travel range for out-of-plane actuators of conventional designs, and the problem of instability risks damaging the devices once collapse happens.

Using a multi-electrode design, He et al. introduced repulsive actuation [19]–[21], which was followed by many researchers [22]–[25]. Pull-in collapse has been successfully overcome, which makes repulsive out-of-plane actuators practical and reliable in a variety of applications needing out-of-plane movements. A cross-section of the electrode layout in repulsive out-of-plane actuators is shown in Fig.1. As demonstrated by the colored electric potential, the movable structure and the fixed center electrode under it are grounded (blue color shows the smallest potential) while the two additional fixed side electrodes are charged with same level of voltage V_s (red color shows the greatest potential). The relative closeness

The authors are with the Department of Mechanical Engineering, Binghamton University, Binghamton, NY 13902, USA (e-mail: ytian30@binghamton.edu; miles@binghamton.edu; stowfigh@binghamton.edu).

of the electric field lines reveals that the upward attractive electric forces, around the upper edge and the top corners of the movable structure, are much more intense than the downward attractive forces around the lower edge of the movable structure [26]. This subtle arrangement of the four electrodes creates net upward electrostatic forces pushing the movable structure away from the substrate (termed repulsive forces).

Theoretical computations and experiments have shown that when we increase the applied side voltages V_s, no pulled-in collapse happens to the actuators and the upward stroke of the movable structure gets larger until the repulsive forces equal the mechanical restoring forces. Movements are allowed within the maximum of achievable strokes, the travel range. The travel range of the out-of-plane repulsive actuators relies on the dimensional parameters as well as the applied voltages. The former decides the effective exertion of actuation and the latter actively actuates the movable structure. For present designs of dimensional parameters, a travel range of 12 microns often needs at least 170V applied [8], [21], [27]. Electrostatic actuators are normally made of polysilicon, which cannot safely employ much higher voltages. Not to mention, when the voltages are generated at such high levels by the electronic circuits, designers face several challenges. The components tend to consume extra-large amounts of power or devote considerably large portions of resources to generate large voltages [28]. Amplified voltages make MEMS devices prone to the simultaneously amplified noise, and the performance of MEMS devices is inevitably hampered [29].

To avoid the drawbacks of high applied voltages, a lot of effort has been put into improving the travel range of out-of-plane actuators at relatively low voltage levels. Increasing the number of repulsive out-of-plane actuators can be effective, but it sacrifices huge areas of micro chips and the increased mass undoubtedly decreases the natural frequencies and then the responding speed of devices. Based on the previous discussion, many works focus on optimizing the dimensional parameters in designs. Lifting the side electrodes instead of fixing them during the out-of-plane motions was demonstrated by Chao et al. [8]. The side-electrode design increased the total repulsive forces because the attractive forces are strengthened and the saturation position was improved slightly. The expenses are more complex electrostatic fields and stronger coupling between active fingers, which bring more challenges to the design of actuators. Towfighian et al. [26] took two consecutive steps to simulate with finite element analysis (FEA) tools, and optimize the dimensional parameters including widths of all four electrodes (W_s, W_c, W_m) as well as the lateral spacing (G_{sc}) to successfully increase the repulsive forces. Chao et al. [30] altered the width of side electrodes, W_s, from constant to double-step values, and that produced a 36% improvement for the travel range of rotation angles.

In the preceding optimization processes, dimensional parameters are often manually adjusted based on researchers' knowledge and experience. Many potential sets of the parameters can be excluded at the same time. It is very possible to miss the global optimal solutions. Thus, there is a need to explore the global solutions to the optimization problem for
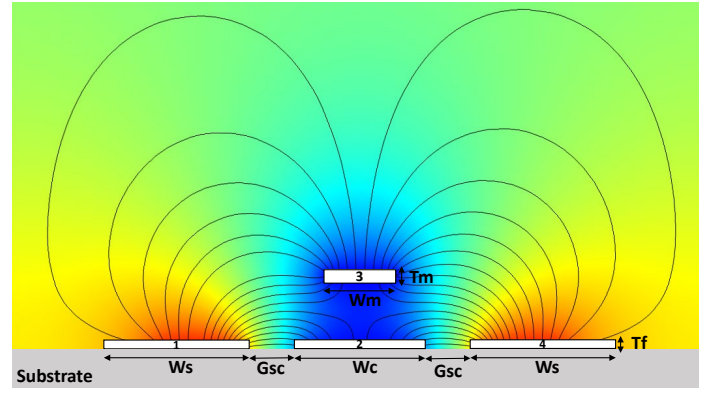

Fig. 1. Cross sectional view of the electrode layout of the repulsive actuation with their dimensional parameters: fixed side electrodes (1 and 4), fixed center electrode (2), and movable structure (3). The geometry is assumed to be uniform in the direction normal to this figure.

enhancing the travel range of out-of-plane actuators.

The main purpose of the present paper is to demonstrate the combination of a boundary element approach with a genetic algorithm to implement a design strategy involving multiple dimensional parameters in a repulsive electrode design. The design parameters shown in Fig.1 (W_s, G_{sc}, W_c, T_f, W_m, T_m) are simultaneously considered and optimized for maximum static displacement at several target voltages V_s. Experimental results are presented showing that the proposed scheme convincingly leads to a design having extended the travel range.

Once a design is obtained that has enhanced travel range, the influence of the optimized dimensional parameters is analyzed for a variety of values of their target voltages for repulsive out-of-plane actuators. This provides a comprehensive understanding of optimization on repulsive out-of-plane actuators and similar multi-electrode systems.

The outline of this paper is as follows: in Section II, the optimization problem is given, and the boundary element/genetic algorithm scheme is proposed. Section III illustrates a case of optimizing travel ranges for a repulsive micro actuator. The experimental setup and methods are described to demonstrate the enlargement of the travel range for the static and dynamic responses. Section IV concludes this article.

II. PROPOSED SCHEME FOR ENLARGEMENT OF ACTUATION RANGE

The optimization problem studied in this article is to maximize the static, out of plane displacement (taken to be the cost function) of the repulsively actuated structure shown in Fig.1 when the side electrodes are charged with voltage V_s. To increase the static displacement, multiple dimensional parameters, listed in Table-I, are gradually varied in a way that is consistent with their constraints imposed by micro fabrication. Finally, the design having these optimized parameters will enable the target voltages to generate a repulsive electric field that produces the largest static displacement possible, meaning the travel range of the actuator reaches its electromechanical limits. The optimization process is shown in Fig.2.

Based on Newton's second law, we can derive a general governing equation of the out-of-plane motion for the movable
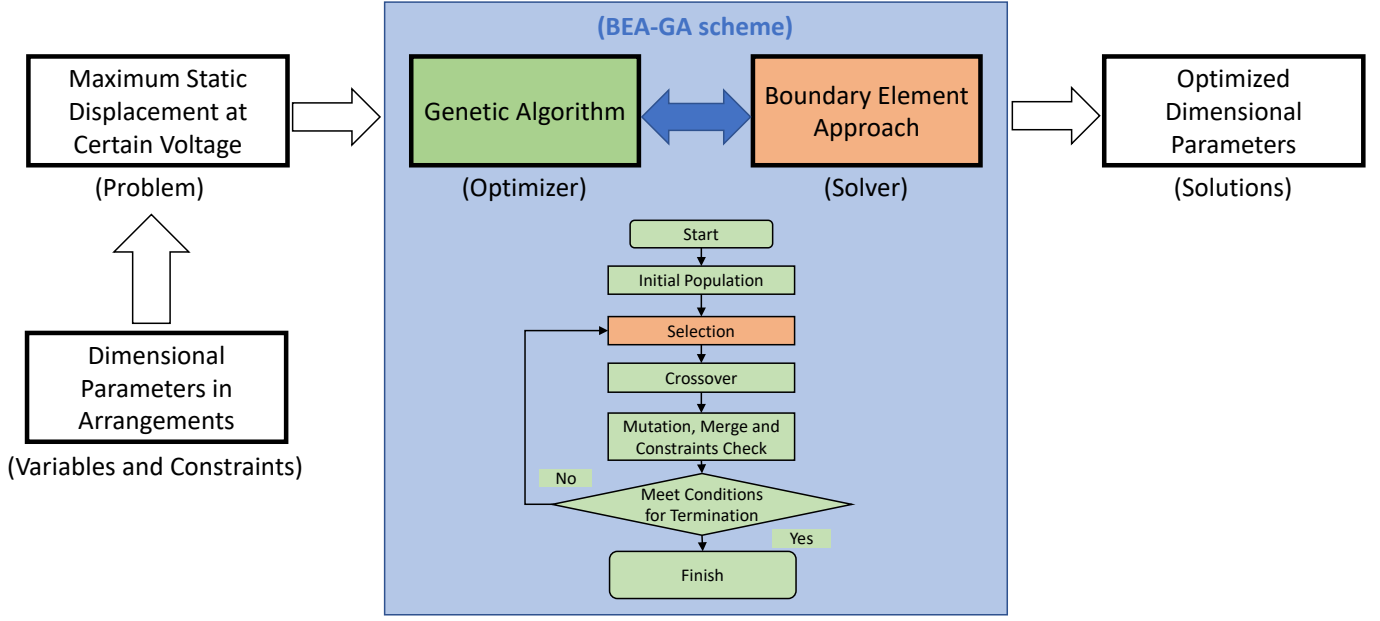
Fig. 2. Overview of the optimization process. The proposed BEA-GA scheme is emphasized in the blue block.

TABLE I
DIMENSIONAL PARAMETERS IN OPTIMIZATION

Variable	Definition
x_1 (W_s)	Width of side electrode
x_2 (G_{sc})	Lateral distance between fixed electrodes
x_3 (W_c)	Width of center electrode
x_4 (T_f)	Thickness of fixed electrodes
x_5 (W_m)	Width of moving electrode
x_6 (T_m)	Thickness of moving electrode

structure under repulsive forces as

$$m_f \ddot{z} = \sum F$$
$$= -c(z) \cdot \dot{z} - k_f(z) \cdot z \qquad (1)$$
$$+ \sum F(z, V_s; W_s, G_{sc}, W_c, T_f, W_m, T_m)$$

where z represents the out-of-plane displacement of the movable structure, m_f is the effective mass, $k_f(z)$ is the effective stiffness function and $c(z)$ is the the damping function. The effective stiffness function $k_f(z)$ can include mid-plane stretching effect for micro clamped-clamped beams [22], clamped-guided beams or stiff plates [24], when large out-of-plane displacements are observed compared to their thicknesses. Also, both the stiffness and damping functions can include nonlinearities that come from the compressibility of the air in the applied environment of very high pressure. $\sum F(z, V_s; W_s, G_{sc}, W_c, T_f, W_m, T_m)$ is the total repulsive force dependent on displacement and V_s and has dimensional parameters described in Table-I.

A. Solver: Boundary Element Approach

The boundary element approach (BEA) was applied to estimate of capacitance in various capacitive microphone designs by Miles [31]. Here, we employ it to model the very nonlinear electric field generated by the layout of the electrodes with their cross-section shown in Fig.1. The boundary element approach is applied to electrodes having the parameters given in Table-III. Electrodes 1 to 4 are discretized having N_1, N_2, N_3 and N_4 finite segments along their edges respectively. After establishing the global coordinates of the segments, we obtain the length as L_i for each tiny segment with midpoint i. After we charge the two fixed side electrodes (1 and 4) and ground the fixed center electrode (2) and the movable structure (3), the electric potential vector can be represented by

$$(V)_{N \times 1} = \begin{pmatrix} (V_1)_{N_1 \times 1} \\ (V_2)_{N_2 \times 1} \\ (V_3)_{N_3 \times 1} \\ (V_4)_{N_4 \times 1} \end{pmatrix} = \begin{pmatrix} (V_s)_{N_1 \times 1} \\ (0)_{N_2 \times 1} \\ (0)_{N_3 \times 1} \\ (V_s)_{N_4 \times 1} \end{pmatrix} \qquad (2)$$

The electric potential on each segment L_i is contributed by all charged segments L_j, including L_i itself. The electric potential on L_i, i.e. v_i, can be computed by

$$v_i = \frac{1}{L_i} \sum_{j=1}^{N} \frac{q_j}{4\pi\epsilon R(i,j)} L_j = \begin{cases} V_s, & 1 \leq i \leq N_1 \\ 0, & 1 \leq i - N1 \leq N_2 \\ 0, & 1 \leq i - N_1 - N_2 \leq N_3 \\ V_s, & others \end{cases} \qquad (3)$$

where $N = \sum_{k=1}^{4} N_k$ is the total number of segments, q_j is the unknown charge on segment L_j, and $R(i,j)$ is the distance between midpoints of L_i and L_j. When domains of summation are two-dimensional, as shown in Fig. 1 and contain only single lines, Eq.3 is given by

$$v_i = \sum_{j=1}^{N} [G]_{ij} q_j = \sum_{j=1}^{N} \begin{cases} -q_j \dfrac{log(R(i,j))}{2\pi\epsilon}, & i \neq j \\ -q_j \dfrac{log(L_i - 1.5)}{2\pi\epsilon}, & i = j \end{cases} \qquad (4)$$

For a detailed derivation of Eq.4, one can refer to [32]. If the movable structure in Fig.1 is a repulsively actuated beam, the
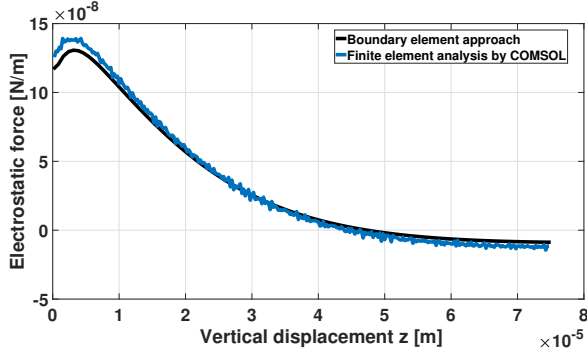
Fig. 3. Electrostatic repulsive force profile for the electrode layout shown in Fig.1 calculated from BEA and the comparison with FEA simulation by COMSOL. Saturation position at around $z_{st} = 45\mu m$ for the dimensional parameters of the previous design given in Table-III.

electrostatic force on it can be calculated as the gradient of electric potential energy multiplied by its length L

$$\sum F(z, V_s; W_s, G_{sc}, W_c, T_f, W_m, T_m)$$
$$= \nabla E(z) \cdot L$$
$$= \nabla \left(\frac{1}{2} (Q)^t (V) \right) \cdot L \qquad (5)$$
$$= \nabla \left(\frac{1}{2} ([G]^{-1}(V))^t (V) \right) \cdot L$$
$$= f(z, V_s; W_s, G_{sc}, W_c, T_f, W_m, T_m) \cdot L$$

where (Q), (V), and $[G]$ represent the charge vector, electric potential vector, and the inverse of capacitance matrix, respectively. We can determine the electric potential energy even if the charge distribution of every segment is unknown. The potential energy function is very important as it reveals forces on the repulsive actuators.

Fig.3 shows how the electrostatic force per length profiles obtained from the boundary element approach and that from a finite element mode by COMSOL are almost identical when $N_1 = N_2 = N_3 = N_4 = 400$. We successfully verified that the boundary element method could provide a sufficiently accurate force per length profile. In addition, boundary element calculation needed 42 seconds while the finite element method provided by COMSOL needed 29 minutes to do the analysis; the boundary element method is much more computationally efficient.

For any set of dimensional parameters, $(W_s, G_{sc}, W_c, T_f, W_m, T_m)$, the repulsive force $\sum F(z, V_s)$ is similarly obtained from the boundary element calculation, fit with a polynomial of the vertical displacement z, and substituted into Eq.1. The static displacement $z_{st} = z_{st}(V_s)$ is obtained by solving the algebraic equation, Eq.6, at a certain supplied V_s with time-dependent terms dropped and regarded as the travel range for each set of dimensional parameters.

$$k_f(z_{st}) \cdot z_{st} = \sum F(z_{st}, V_s; W_s, G_{sc}, W_c, T_f, W_m, T_m) \quad (6)$$

B. Optimizer: Genetic Algorithm (GA)

We investigated the suitability and reliability of approaches to simultaneously optimize multiple dimensional parameters listed in Table I to maximize the static displacement $z_{st}(V_s)$. As this is a derivative-free optimization problem with constrained and multi-objective coupling, several optimization techniques such as hybrid simulated annealing, generalized pattern search, particle swarm optimization, and genetic algorithm (GA) are popularly deployed. Our research determined that GA is the most suitable optimizer for our problem as it globally searches for solutions with more efficiency, robustness, and stability [33].

We first pick a target voltage, V_s. We expect that the optimized solutions should perform best at that applied voltage. As the GA works according to the flow shown in Fig.2, it first randomly generates some initial population, $I_0=(W_s, G_{sc}, W_c, T_f, W_m, T_m)_0$, within the constraints of the dimensional parameters. After the initialization, GA calls BEA to solve the static displacement $z_{st,0}(V_s)$ at the target V_s for every individual, and they are regarded as their fitness values. In the following two cases, we will give more details of constraints along with their target voltages. Based on the fitness values, we assign each individual a probability of being kept for the next operations. This step uses roulette wheel selection, and the probability of selecting each individual I_k^i in k^{th} generation (k=0,1,2,..) is

$$\mathbf{P}\{I_k^i\} = \frac{z_{st,k}^i(V_s)}{\sum z_{st,k}^i(V_s)} \qquad (7)$$

which secures individuals I_k^i with greater fitness values $z_{st,k}^i(V_s)$ are more likely to be selected than individuals with lesser fitness values. The selected parents will crossover and create the next generation of individuals, the offspring I_1, which are presumably better than the parents I_0 as long as we have enough individuals. We then add some mutations to the offspring. Extra population are also generated from the merging of them with their parents I_0. After we conduct all the preparations and generate enough individuals as I_1, we need to check and adjust to ensure the I_1 remain constrained. BEA is called again to solve Eq.6 for dimensional parameters, I_1, and new parents I_2 are selected again based on their fitness values, $z_{st,1}(V_s)$. GA is an iterative process that repeats all of the preceding steps until the prescribed number of iterations is reached. The optimal result after each iteration m is recorded as $max(z_{st,k}(V_s))$. Here we set the final generation as the 100th generation and the solutions $I_{100}=(W_s, G_{sc}, W_c, T_f, W_m, T_m)_{100}$ are output as optimized dimensional parameters which gives optimized displacement $max(z_{st,100}(V_s))$ at the target voltage V_s.

III. OPTIMIZATION FOR ENHANCING TRAVEL RANGES

In practical design optimization problems for out-of-plane actuators, most constraints involve the processes in micro fabrication. For example, dimensions or differences of two overlapping dimensions must have certain values, which avoids misalignment-caused fabrication defects. In this paper, constraints of the dimensional parameters will primarily include fabrication rules by PolyMUMPs [34]. The constraints are listed in Table-III. The exact values of all thicknesses and minimum difference between W_c and W_m are ruled by PolyMUMPs. Other constraints assume a sufficient area

on the chip for fabricating the out-of-plane actuators (micro cantilever) and, to enlarge the travel range of the out-of-plane actuator, any reasonable values of dimensional parameters within the generous limitations are acceptable. PolyMUMPs is a developed and commercially available process offering successful yields and small fabrication costs, and we will use products by PolyMUMPs to experimental verify most static and dynamic results.

The proposed BEA-GA scheme is applied to a micro cantilever actuator with repulsive forces. For a cantilever of length L (properties listed in Table-II) modeled with the Bernoulli-Euler beam theory, the governing equation Eq.1 can be defined as

$$
\rho A \frac{\partial^2 z}{\partial t^2} + c^* \frac{\partial z}{\partial t} + EI \frac{\partial^4 z}{\partial x^4}
$$
$$
+ V_s^2 f_e(z; W_s, G_{sc}, W_c, T_f, W_m, T_m) = 0 \tag{8}
$$

where out-of-plane displacement z is related to the position along the length of the beam, x, and time, t. $A = W_m \cdot T_m$ is the area of the cross-section. The displacement of the cantilever beam is assumed to be product of first mode shape, $\phi(x)$, and time-dependent function as shown

$$
z(x,t) = \phi(x) \cdot q(t)
$$
$$
\phi(x) = cosh(\lambda x) - cos(\lambda x) - \mu(sinh(\lambda x) - sin(\lambda x))
$$
$$
\mu = \frac{sinh(\lambda L) - sin(\lambda L)}{cosh(\lambda L) + cos(\lambda L)}
$$
$$\tag{9}$$

After separation of variables, the governing equation of the beam, Eq.8, is multiplied by $\phi(x)$ and integrated over x from 0 to L to yield the general form as

$$
m_f \ddot{q} = \sum F
$$
$$
= - c \cdot \dot{q} - k_f \cdot q
$$
$$
+ V_s^2 F_e(q; W_s, G_{sc}, W_c, T_f, W_m, T_m) \tag{10}
$$

where the effective mass m_f, effective stiffness k_f and the damping c are given in Eq.11 and Q is the quality factor. F_e is the electrostatic force related to specific dimensional parameters, $(W_s, G_{sc}, W_c, T_f, W_m, T_m)$.

$$
m_f = \rho A \int_0^L \phi^2(x)dx
$$
$$
k_f = EI \int_0^L \phi''''(x)\phi(x)dx
$$
$$
c = c^* \int_0^L \phi^2(x)dx = \frac{k_f}{Q} \tag{11}
$$
$$
F_e(q; W_s, G_{sc}, W_c, T_f, W_m, T_m)
$$
$$
= \int_0^L f_e(q; W_s, G_{sc}, W_c, T_f, W_m, T_m) \cdot \phi(x)dx
$$

As described in II-A, we write the static governing equation after eliminating the time-dependent terms in Eq.10 as

$$
k_f \cdot q_{st} + V_s^2 F_e(q_{st}; W_s, G_{sc}, W_c, T_f, W_m, T_m) = 0 \tag{12}
$$

Now that the travel range can be obtained as the static displacement at the tip of the beam as $z_{st} = \phi(L) \cdot q_{st}$, optimization is conducted to enlarge the travel range for this

TABLE II
BEAM MATERIAL AND GEOMETRIC PROPERTIES

Property	Symbol	Value
Cantilever length (μm)	L	500
Density (kg/m^3)	ρ	2330
Elastic modulus (GPa)	E	150
Beam-center electrode gap (μm)	d	2

TABLE III
DIMENSIONAL PARAMETERS OF MICRO ACTUATOR AND CONSTRAINTS
(UNIT: μm)

Variable	Constraints	Previous design	Optimized design 1	Optimized design 2
x_1 (W_s)	$4 \leq W_s \leq 38$	28	38	38
x_2 (G_{sc})	$4 \leq G_{sc} \leq 25$	20.5	4	4
x_3 (W_c)	$8 \leq W_c - W_m \leq 25$	12.5	8	8
x_4 (T_f)	$T_f = 0.5$	-	-	-
x_5 (W_m)	$10 \leq W_m \leq 25$	17.5	10	17.5
x_6 (T_m)	$T_f = 2$	-	-	-

micro actuator. For optimization, the target voltages are set to values from $V_s = 40V$ to $V_s = 140V$ with a step of 20V. The BEA-GA optimization ensures the maximum travel range for the micro-cantilever when the voltage for each step is applied to the side electrodes. Optimization is conducted six times for the six target voltages and the optimized dimensional parameters are recorded. Four runs of BEA-GA optimization out of many trials of target voltage $V_s = 120V$ are shown in Fig.6 and demonstrate that 100 iterations are quite adequate to converge to the optimized design 1 in III. The convergent situation is similar for the other target voltages.

Our investigation reveals that when the target voltages vary from $V_s = 40V$ to $V_s = 140V$ with a step of 20V, the solutions are identical to be the optimized design 1 in Table-III. The optimized dimensional parameters I_{100} are maximizing the width of side electrodes W_s while minimizing all of the other parameters to the boundary values. The optimized dimensional parameters are reasonable as they establish a much more compact electrostatic field in which the provider of repulsive forces, side electrodes, are maximized.

After those steps, we require to preserve the size of the micro actuator, i.e. fixing the value of W_m, and re-do the optimization for the target voltages from $V_s = 40V$ to $V_s = 140V$ with a step of 20V. We build optimized design 2 as the optimal solution for all target voltages. Fig.4 shows the repulsive force profiles for the previous design, optimized design 1 and optimized design 2. The figure shows the optimized dimensional parameters substantially improve the electrostatic forces in a range of vertical displacement between $0\mu m$ and $17\mu m$, which is the applicable range for micro cantilevers. At the same time, the saturation position where the force vanishes is decreased from $45\mu m$ to $30\mu m$. It is still far away from the usable range so it is not concerning.

IV. EXPERIMENTAL RESULTS

New chips with beams of optimized design 1 and optimized design 2 were fabricated to the PolyMUMPs standard and a comparison of the dimensional parameters with our previous design is shown in Fig.5. Beams as tiny as $10\mu m$ wide are made and are fabricated with small chamfers on both sides of the fixed end to make them less vulnerable to break.
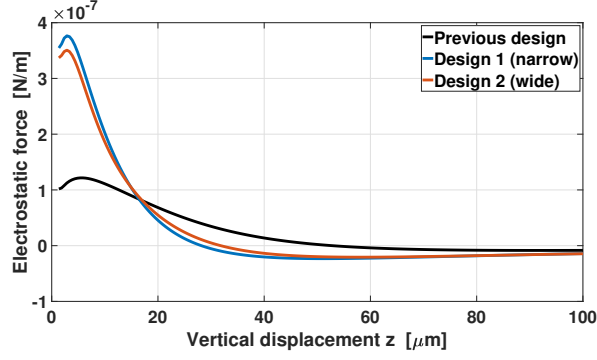
Fig. 4. Comparison of electrostatic repulsive force profiles for the electrode layouts of three designs in Table-III.
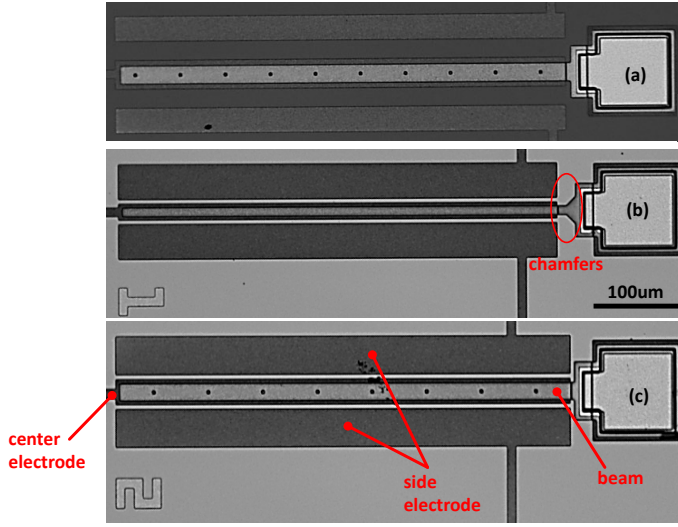

Fig. 5. Comparison of microscopic views of the fabricated cantilever beams of: (a) previous design (17.5μm-wide); (b) optimized design 1 (10μm-wide); and (c) optimized design 2 (17.5μm-wide). Beams are 500 um long. Red lines indicate the components of the electrode layout as in Fig.1 and the red circle indicates the chamfers added for the narrow beam.
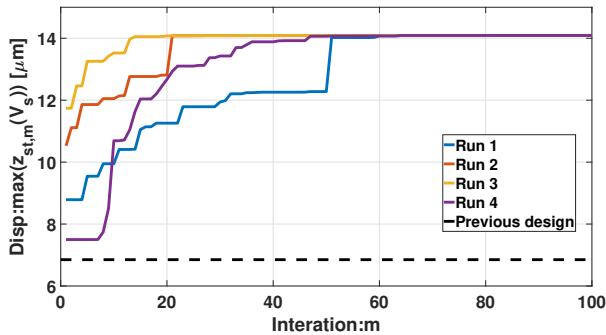

Fig. 6. Records of iterations versus displacement output after every GA step. Target voltage V_s is 120V.

TABLE IV
ADJUSTED VALUES AND RATE OF ADJUSTMENT

Item	Value	Standard value	Rate of adjustment (%)
Design 1: L (μm)	495	500	-1%
Design 1: Tm (μm)	1.8	2	-10%
Design 1: λL	1.98	1.875	-5.6%
Design 2: L (μm)	505	500	+1%
Design 2: Tm (μm)	1.82	2	-9%
Design 2: λL	1.97	1.875	-5.1%

Thus, as can be seen in Fig.5, the actuated length of the $10\mu m$-wide beam is slightly smaller than $500\mu m$. Because both of the new beams (b)(c) are very long, inevitable initial curling from residual stress happens when the beams are released in micro fabrication. Also, the connection to an anchor is not a perfectly fixed constraint so the hanging parts should be considered to adjust the length of the beam model. One effective way to account for the initial curvature of the structures and imperfections from fabrication and make the established theoretical model fit well with the experiments, is to slightly adjust the natural frequency number, λL, in Eq.9 [35], lengths and thicknesses. The adjustment taken here is listed and compared with standard value of cantilever beams as in Table-IV

A. Enhanced static response

The chip is placed in a vacuum chamber and the static displacements versus varying side voltages of the cantilever beams are measured with a Polytec MSA-500 laser vibrometer as in Fig.7. The theoretical static displacements from Eq.6 are in good agreement with tip-measured experimental data. There is a significant enlargement of the travel range for the six steps in voltage from 40V to 120V compared with the previous design. Optimized design 2 provides a travel range with 49% to 130% improvement, and optimized design 1 achieves an unprecedented enlargement of 105% to 192%. The improved travel ranges suggest that we can use much lower supplied voltages, i.e. 80V, to accommodate the same level of behaviors that had required 140V as applied voltage level by the previous design.

Before conducting experimental measurement for the dynamic tests, we need to determine the fundamental natural frequencies of the actuators. The theoretical natural frequencies are computed from the eigenvalues of the Jacobian of Eq.1 at the displacement in Fig.7. In the chamber, the air pressure P_a is reduced to approximately 300mtorr. Side voltages from 40V to 140V are applied with a small white random noise to the side electrodes. The velocity measurements are taken by Polytec MSA-500 laser vibrometer at around $30\mu m$ from the anchor of the micro actuators and a fast Fourier transformation is used to the signal and the fundamental natural frequencies are recorded as in Fig.8. The theoretical and experimental results of natural frequencies show an increasing trend as the applied side voltages are increased. Optimized design 1 and optimized design 2 have much higher natural frequencies than the previous design, which is a result that the electrostatic forces are greatly strengthened by the dimensional parameters after optimization.
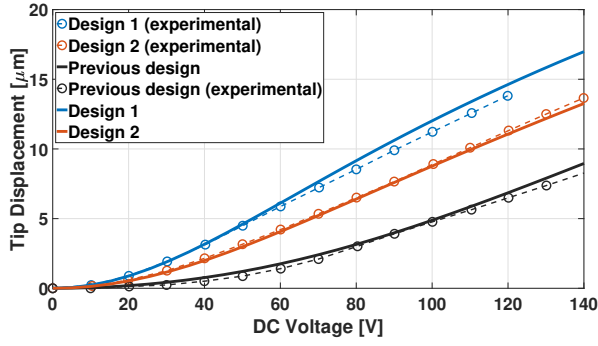
Fig. 7. Static tip displacements of the micro actuators versus applied side voltages V_s. Solid lines indicate theoretical results and circles indicate displacements measured under the vibrometer. The location of the measurement is approximately $30\mu m$ from the tip of the micro actuators.
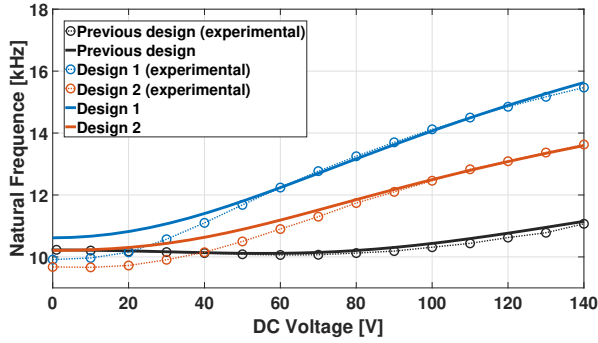

Fig. 9. Theoretical fundamental resonance at $V_{dc} = 120V$ and $V_{ac} = 0.5V$ and an air pressure $P_a = 300mtorr$.

Fig. 8. Changes in the fundamental natural frequencies with applied side voltages V_s. Solid lines and circles with dotted lines indicate the theoretical and experimental results, respectively. The location of the measurement is approximately $30\mu m$ from the tip of the micro actuators.

Fig. 10. Fundamental resonance at $V_{dc} = 120V$ and $V_{ac} = 0.5V$ and an air pressure $P_a = 300mtorr$. Solid lines indicate theoretical results and experimental data measured under vibrometer in backward frequency sweeping (squares) and forward frequency sweeping (stars). Quality factors, Q, for design 1 and design 2 are 200 and 500.

B. Enhanced dynamic responses

1) Fundamental resonance: The enlarged travel ranges allow much larger vibrating amplitudes for dynamic applications of the micro actuators. The theoretical dynamic amplitudes in fundamental resonance for previous design, optimized design 1 and optimized design 2 are calculated by solving Eq.1 with long-time integration in MATLAB, shown in Fig.9. During the measurement of dynamic resonant responses, a pressure $P_a =$ 300mtorr and side voltages $V_s = V_{dc} + V_{ac}cos(\Omega t)$ were used in the forward and backward frequency sweeping. The displacements were recorded around $30\mu m$ from the tip and compared with the theoretical results shown in Fig.10. With a significantly enlarged travel range, optimized design 1 can accommodate a 110% larger dynamic amplitude and optimized design 2 allows an 81% improved dynamic amplitude. Those high amplitudes were not obtained with the previous design. Even though there is a slight difference between the bandwidth of theoretical results and experimental data, the theoretical results predict the allowed amplitudes very efficiently. Improving the effective terms in Eq.11 to include more modes can improve the agreement.

2) Principal parametric resonance: Principle parametric resonance is another distinct mechanism of excitation for out-of-plane actuators and happens when the driving frequencies
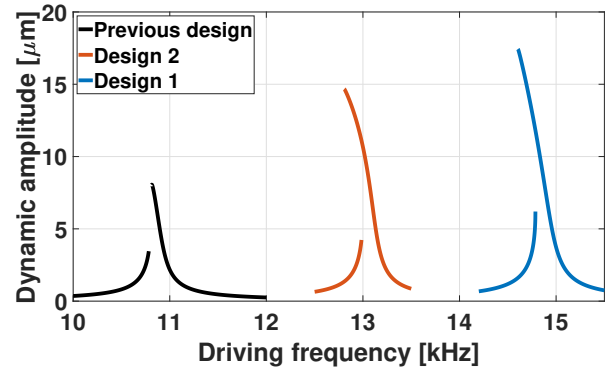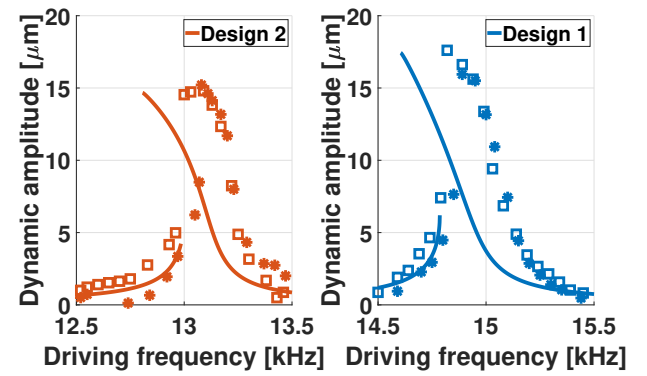
are close to twice the natural frequencies. Because of the significantly large amplitudes and less dependence on damping in the environments, it has been extensively investigated for out-of-plane actuators. In previous works, voltages needed by repulsive actuators of the same size to establish a large enough travel range to accommodate parametrically resonated amplitudes as large as $10\mu m$ are often greater than 165V [23], [36]. With theoretical amplitudes and experimentally measured data from the new chips in Fig.11, we observe an enlarged accommodation of $10\mu m$ parametric excitation with applied side voltages as low as 80V. Large amplitudes at significantly smaller voltages allow actuators to obtain greatly-improved signal-to-noise ratios, which vastly improves the sensing and actuation capabilities of many applications.

It is valuable to mention that with such low side voltages applied, dynamic amplitudes grow significantly. The parametrically resonated beams will get very close to the substrate. To predict the amplitudes, we need to consider the nonlinear damping and stiffness caused by the compressed air under the beam [23]. The squeeze-film damping effect is extensively described in [37] and the nonlinear air spring and air damping
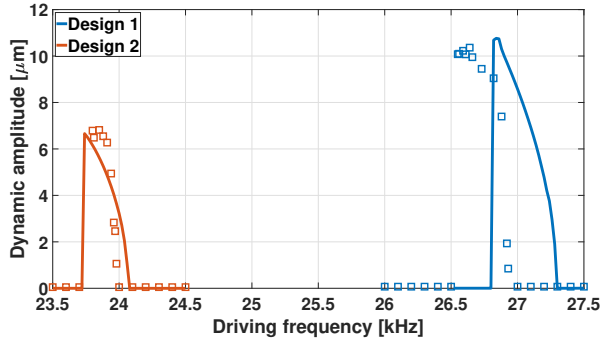
Fig. 11. Principal parametric resonance at $V_{dc} = 80V$ and $V_{ac} = 0.5V$ and an air pressure $P_a = 300mtorr$. Solid lines indicate theoretical results in backward sweeping and squares represent experimental data measured under vibrometer in backward frequency sweeping. No parametric resonance is available in previous design at these voltages.

terms are given by

$$
k_{air}(z) = \frac{64\sigma^2 P_a(L \cdot W_m)}{\pi^8(z+d)} \frac{1}{\left(1+(\frac{W_m}{L})^2\right)^2 + \frac{\sigma^2}{\pi^4}}
$$
$$
c_{air}(z) = \frac{64\sigma P_a(L \cdot W_m)}{\pi^6 \Omega(z+d)} \frac{1+(\frac{W_m}{L})^2}{\left(1+(\frac{W_m}{L})^2\right)^2 + \frac{\sigma^2}{\pi^4}}
\tag{13}
$$

where P_a is the air pressure, Ω is the oscillation frequency and σ is the squeeze number defined as

$$
\sigma = \frac{12(L \cdot W_m)\Omega\mu_f}{P_a(z+d)^2}
\tag{14}
$$

where μ_f is the effective viscosity of the air and equals 1.0464×10^{-8} when Pa is 300mtorr. The nonlinear air spring will provide additional stiffness besides the mechanical stiffness in Eq. 11 and the nonlinear air damping will be dominant and replace the linear damping in Eq. 11. Because the analytical expression in Eq. 13 is obtained with assumption of compressed air in a very large area, they can predict the response of the wider beam (optimized design 2) much better than the thinner beam (optimized design 1). Nevertheless, one can observe that the theoretical amplitudes predict the allowed amplitudes very well for the parametric resonance. To improve the match, one can take the nonlinear forms of the spring and damping in the squeeze-film damping model and identify the coefficients from experimental data [23].

V. Conclusion

In this paper, a methodology combining the boundary element approach (BEA) and genetic algorithm (GA) was proposed to enlarge the travel range of the out-of-plane micro actuator with repulsive actuation. BEA acted as an efficient and accurate solver of electrostatic forces for nonlinear electric fields. The travel ranges were calculated by solving the nonlinear equations exploiting the nonlinear terms appearing in large movements. Based on the results, GA was splendidly employed for optimizing the dimensional parameters globally at different target voltages. Our theoretical and experimental results demonstrate that for micro actuator beams with optimized dimensional parameters, travel ranges can be enlarged

by 40% to 130% from the previous design. Accommodated dynamic amplitudes in fundamental resonance and principal parametric resonance verified the significant improvement of travel ranges. This proposed scheme and the explanation of enhancing travel ranges are useful for all MEMS designs that benefit from repulsive actuation.

References

[1] M. Pallay, R. N. Miles, and S. Towfighian, "A tunable electrostatic mems pressure switch," *IEEE Transactions on Industrial Electronics*, vol. 67, no. 11, pp. 9833–9840, 2019.

[2] S. K. Waghmare and D. Shah, "Rf mems capacitive shunt switch: a study based practical overview," *Int J Appl Eng Res*, vol. 13, no. 15, pp. 11 830–11 838, 2018.

[3] K. Isamoto, K. Kato, A. Morosawa, C. Chong, H. Fujita, and H. Toshiyoshi, "A 5-v operated mems variable optical attenuator by soi bulk micromachining," *IEEE Journal of selected topics in quantum electronics*, vol. 10, no. 3, pp. 570–578, 2004.

[4] L. Li, J. Zawadzka, and D. Uttamchandani, "Integrated self-assembling and holding technique applied to a 3-d mems variable optical attenuator," *Journal of microelectromechanical systems*, vol. 13, no. 1, pp. 83–90, 2004.

[5] P. Ashok Kumar, S. R. Karumuri, G. S. Kondavitee, and K. Guha, "Design and performance analysis of a low-pull-in-voltage rf mems shunt switch for millimeter-wave therapy, iot, and 5g applications," *Journal of Computational Electronics*, pp. 1–8, 2022.

[6] U. Hofmann, J. Janes, and H.-J. Quenzer, "High-q mems resonators for laser beam scanning displays," *Micromachines*, vol. 3, no. 2, pp. 509–528, 2012.

[7] A. D. Yalcinkaya, H. Urey, D. Brown, T. Montague, and R. Sprague, "Two-axis electromagnetic microscanner for high resolution displays," *Journal of Microelectromechanical Systems*, vol. 15, no. 4, pp. 786–794, 2006.

[8] C. Fan and S. He, "A two-row interdigitating-finger repulsive-torque electrostatic actuator and its application to micromirror vector display," *Journal of Microelectromechanical Systems*, vol. 24, no. 6, pp. 2049–2061, 2015.

[9] K. F. Chan, Z. Feng, R. Yang, A. Ishikawa, and W. Mei, "High-resolution maskless lithography," *Journal of Micro/Nanolithography, MEMS, and MOEMS*, vol. 2, no. 4, pp. 331–339, 2003.

[10] I. W. Jung, J.-S. Wang, and O. Solgaard, "Optical pattern generation using a spatial light modulator for maskless lithography," *IEEE Journal of Selected Topics in Quantum Electronics*, vol. 13, no. 2, pp. 147–154, 2007.

[11] D.-H. Dinh, H.-L. Chien, and Y.-C. Lee, "Maskless lithography based on digital micromirror device (dmd) and double sided microlens and spatial filter array," *Optics & Laser Technology*, vol. 113, pp. 407–415, 2019.

[12] K. Banerjee, P. Rajaeipour, H. Zappe, and Ç. Ataman, "A 37-actuator polyimide deformable mirror with electrostatic actuation for adaptive optics microscopy," *Journal of Micromechanics and Microengineering*, vol. 29, no. 8, p. 085005, 2019.

[13] D. J. Dagel, W. D. Cowan, O. B. Spahn, G. D. Grossetete, A. J. Grine, M. J. Shaw, P. J. Resnick, and B. Jokiel, "Large-stroke mems deformable mirrors for adaptive optics," *Journal of Microelectromechanical Systems*, vol. 15, no. 3, pp. 572–583, 2006.

[14] T. Liu, A. J. Svidunovich, B. C. Wollant, and D. L. Dickensheets, "Mems 3-d scan mirror with su-8 membrane and flexures for high na microscopy," *Journal of Microelectromechanical Systems*, vol. 27, no. 4, pp. 719–729, 2018.

[15] V. Milanovic, G. A. Matus, and D. T. McCormick, "Gimbal-less monolithic silicon actuators for tip-tilt-piston micromirror applications," *IEEE journal of selected topics in quantum electronics*, vol. 10, no. 3, pp. 462–471, 2004.

[16] J. I. Seeger and B. E. Boser, "Charge control of parallel-plate, electrostatic actuators and the tip-in instability," *Journal of Microelectromechanical systems*, vol. 12, no. 5, pp. 656–671, 2003.

[17] R. Nadal-Guardia, A. Dehe, R. Aigner, and L. Castaner, "Current drive methods to extend the range of travel of electrostatic microactuators beyond the voltage pull-in point," *Journal of microelectromechanical systems*, vol. 11, no. 3, pp. 255–263, 2002.

[18] E. K. Chan and R. W. Dutton, "Electrostatic micromechanical actuator with extended range of travel," *Journal of microelectromechanical Systems*, vol. 9, no. 3, pp. 321–328, 2000.

[19] S. He and R. B. Mrad, "Large-stroke microelectrostatic actuators for vertical translation of micromirrors used in adaptive optics," *IEEE Transactions on Industrial Electronics*, vol. 52, no. 4, pp. 974–983, 2005.

[20] S. He and R. B. Mrad, "Design, modeling, and demonstration of a mems repulsive-force out-of-plane electrostatic micro actuator," *Journal of Microelectromechanical Systems*, vol. 17, no. 3, pp. 532–547, 2008.

[21] S. He, R. B. Mrad, and J. Chong, "Repulsive-force out-of-plane large stroke translation micro electrostatic actuator," *Journal of Micromechanics and Microengineering*, vol. 21, no. 7, p. 075002, 2011.

[22] M. Pallay, M. Daeichin, and S. Towfighian, "Dynamic behavior of an electrostatic mems resonator with repulsive actuation," *Nonlinear Dynamics*, vol. 89, no. 2, pp. 1525–1538, 2017.

[23] M. Pallay and S. Towfighian, "A parametric electrostatic resonator using repulsive force," *Sensors and Actuators A: Physical*, vol. 277, pp. 134–141, 2018.

[24] M. Ozdogan, M. Daeichin, A. Ramini, and S. Towfighian, "Parametric resonance of a repulsive force mems electrostatic mirror," *Sensors and Actuators A: Physical*, vol. 265, pp. 20–31, 2017.

[25] Y. Tian, M. Daeichin, and S. Towfighian, "Dynamic behavior of t-beam resonator with repulsive actuation," *Nonlinear Dynamics*, vol. 107, no. 1, pp. 15–31, 2022.

[26] S. Towfighian, S. He, and R. Ben Mrad, "A low voltage electrostatic micro actuator for large out-of-plane displacement," in *International Design Engineering Technical Conferences and Computers and Information in Engineering Conference*, vol. 46353, p. V004T09A015. American Society of Mechanical Engineers, 2014.

[27] J. Chong, S. He, and R. B. Mrad, "Development of a vector display system based on a surface-micromachined micromirror," *IEEE Transactions on Industrial Electronics*, vol. 59, no. 12, pp. 4863–4870, 2011.

[28] M. Marx, S. Rombach, S. Nessler, D. De Dorigo, and Y. Manoli, "A 141-¡inline-formula¿ ¡tex-math notation="latex"¿μ ¡/tex-math¿¡/inline-formula¿w high-voltage mems gyroscope drive interface circuit based on flying capacitors," *IEEE Journal of Solid-State Circuits*, vol. 54, DOI 10.1109/JSSC.2018.2875109, no. 2, pp. 511–523, 2019.

[29] M. Agarwal, K. Park, M. Hopcroft, S. Chandorkar, R. Candler, B. Kim, R. Melamud, G. Yama, B. Murmann, and T. Kenny, "Effects of mechanical vibrations and bias voltage noise on phase noise of mems resonator based oscillators," in *19th IEEE international conference on micro electro mechanical systems*, pp. 154–157. IEEE, 2006.

[30] C. Fan and S. He, "A microelectrostatic repulsive-torque rotation actuator with two-width fingers," *Journal of Micromechanics and Microengineering*, vol. 25, no. 9, p. 095006, 2015.

[31] R. N. Miles, "Estimation of capacitance," in *Physical Approach to Engineering Acoustics*, pp. 307–329. Springer, 2020.

[32] T. Li, "3d capacitance extraction with the method of moments," Ph.D. dissertation, Worcester Polytechnic Institute, 2010.

[33] M. Melnyk, A. Kernytskyy, M. Lobur, M. Szermer, P. Zajac, and W. Zabierowski, "Application of a genetic algorithm for dimension optimization of the mems-based accelerometer," in *Proceedings of the 20th International Conference Mixed Design of Integrated Circuits and Systems-MIXDES 2013*, pp. 352–354. IEEE, 2013.

[34] A. Cowen, B. Hardy, R. Mahadevan, and S. Wilcenski, "Polymumps design handbook," *Memscap Inc*, vol. 13, 2011.

[35] M. Pallay, R. N. Miles, and S. Towfighian, "Merging parallel-plate and levitation actuators to enable linearity and tunability in electrostatic mems," *Journal of Applied Physics*, vol. 126, no. 1, p. 014501, 2019.

[36] M. Pallay, M. Daeichin, and S. Towfighian, "Feasibility study of a micro-electro-mechanical-systems threshold-pressure sensor based on parametric resonance: experimental and theoretical investigations," *Journal of Micromechanics and Microengineering*, vol. 31, no. 2, p. 025002, 2020.

[37] M. I. Younis, *MEMS linear and nonlinear statics and dynamics*, vol. 20. Springer Science & Business Media, 2011.

Yu Tian received the M.S. in mechanical engineering in 2021 from Binghamton University, where he is currently working towards as Ph.D. in mechanical engineering with the MEMS and Energy Harvesting Laboratory. His research focuses on MEMS, sensors and actuators, mechanical vibrations, and nonlinear dynamics.

Ronald N. Miles received the B.S. degree in electrical engineering from the University of California at Berkeley, Berkeley, CA, USA, and the M.S. and Ph.D. degrees in mechanical engineering from the University of Washington. He has been with the Department of Mechanical Engineering, the State University of New York at Binghamton (SUNY Binghamton), Binghamton, NY, USA, since 1989. He has served as the Director for Graduate and Undergraduate Studies, an Associate Chair, a Professor, a Distinguished Professor, an Associate Dean for Research and the Chair for the Department of Mechanical Engineering.

Shahrzad Towfighian received her PhD degree in Mechanical Engineering from the University of Waterloo, Canada in 2011. She joined the Mechanical Engineering department at Binghamton University in Fall 2013. Her research interests include Micro-electro-mechanical sensors/actuators and energy harvesting. She develops mathematical models of electro-mechanical systems to predict their behavior. She discovers new ways of sensing and actuation for improving functionality of MEMS devices.